



OPEN

Rapid and sensitive magnetic field sensor based on photonic crystal fiber with magnetic fluid infiltrated nanoholes

Saeed Azad^{1,4}, Satyendra Kumar Mishra², Ghasem Rezaei³, Ricardo Izquierdo^{1,4} & Bora Ung^{1,4}✉

A fast response time (0.1 s) magnetic field sensor has been demonstrated utilizing a photonic crystal fiber with nano-size air holes infiltrated with polyethylene glycol based magnetic fluid. The effect of magnetic nanoparticles concentration in the fluid on the magneto-optical sensor performance and its dependence under varying magnetic-field loads was investigated in detail. In particular, the sensor response was analytically modelled with a Langevin function with a good fit ($R \geq 0.996$). A threshold sensing point as low as 20 gauss was recorded and a detection range of 0–350 gauss was demonstrated by means of optical transmission measurements. The experimental results were validated by theory using a waveguide light transmission model fed by finite-element method simulations of the principal guided modes in the infiltrated fiber sensor. The simple interrogation scheme, high sensitivity and quick response time makes the proposed hybrid fiber-optic magneto-fluidic probe a promising platform for novel biochemical sensing applications.

With the advent of the internet of things, wearable sensors and personalized medicine, there is growing demand for compact and reliable sensors to provide biosensing and environmental monitoring to users and artificially intelligent beings. Among various kinds of optical fiber based sensors, specialty fibers infiltrated with magnetic fluid has recently attracted scrutiny towards the development of highly sensitive and compact magnetic field sensors. Magnetic field sensors have been extensively used in electric current measurements, in metallurgy, power industry, in biomedical detection, for the oil and gas exploration as well as aviation industry^{1–3}. The most common methods rely on magneto-transistor, magneto-resistive, fluxgate or the Hall effect to detect and measure magnetic fields^{4–6}. These sensors exhibit some drawbacks related to their power consumption, limited multiplexing, cost, miniaturization and remote monitoring capabilities. In addition, surrounding electrical field sources are prone to introduce noise via electromagnetic interference to the electronic circuits⁷.

Compared to conventional sensors, optical fiber based magnetic field sensors offer promising key benefits such as a compact size, immunity to electromagnetic interference, remote monitoring and multiplexing capabilities through optical networks modalities, high reliability and sensitivity. Initial fiber-optic magnetic field sensors reported in the last four decades employed magnetostrictive materials in conjunction with Mach–Zehnder interferometry while other schemes exploit changes on the state of polarization of the light^{8–11}.

Meanwhile with the growth of nanotechnology and the advent of liquids functionalized with nanoparticles, emerging applications of so called magnetic fluids (MF) are studied in the sensing field. A MF is a liquid typically composed of single-domain magnetic nanoparticles (MNPs) coated with surfactant in suspension within a liquid carrier, and with engineered physicochemical properties including magnetic susceptibility, polydispersity, and dipolar interactions. Owing to its customizable magneto-optical properties, MFs have been applied in a variety of photonic devices, including optical gratings¹², optical switches¹³, modulators¹⁴, couplers¹⁵ and magnetic field sensors¹⁶.

The ability to exhibit a magnetic-field-dependent refractive index (RI)^{17,18} that is attributed to the microstructural distribution of MNPs inside the MF is a key parameter used in many sensing applications. Accordingly, different configurations of optical fibers in conjunction with MF have been well studied as magnetic field sensors.

¹Department of Electrical Engineering, École de technologie supérieure, Montreal H3C 1K3, Canada. ²Université Laval, Center for Optics, Photonics and Lasers (COPL), Quebec G1V 0A6, Canada. ³Department of Physics, College of Sciences, Yasouj University, Yasouj 75918-74934, Iran. ⁴Department of Electrical Engineering, LACIME, Montreal H3C 1K3, Canada. ✉email: bora.ung@etsmtl.ca

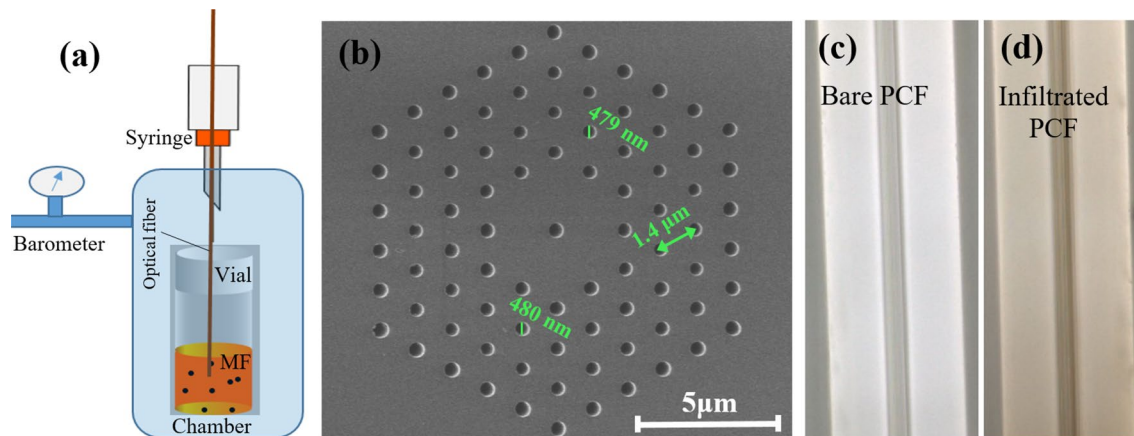


Figure 1. (a) Schematic of experimental setup for filling the PCF, (b) Cross section SEM image of PCF, (c) Optical microscope image of Bare PCF and (d) infiltrated side views of the PCF.

They can be used in three different configurations, initially in the form of the MF thin film at the end facet of optical fiber cross section, as the cladding of an etched/tapered fiber (in the middle section) and finally as the filling material inside the fiber. For the first configuration, several Fabry–Pérot based sensors that incorporate MF within a section of optical fiber were reported^{19,20}. This technique suffers from sensitivity to thermal expansion and a complicated process to calculate and fabricate the correct cavity dimensions. Those problems were solved in etched tapered fibers^{21,22}, however these thinned fibers are very fragile owing to their low mechanical strength. Finally, by injecting the MF inside the fiber, the original microstructured features are not only preserved but the whole fiber also offers an extended interaction area that enhances the sensitivity²³. In this work, we present a special photonic crystal fiber (PCF) with nanometer-scale air holes infiltrated with MF. Sensor performances including sensitivity, threshold and saturation points, response/recovery times were studied in detail for various concentrations of the MF. This work is organized as follow: section “[Fabrication process and operation principle](#)” describes the PCF infiltration process and sensing principle. In section “[Results and discussion](#)” the experimental investigation on the effect of MF concentrations in sensor responses are considered. Also, numerical simulations regarding output power, which is then followed by a comparison between the experimental and simulation results were done. The proposed functional sensor with features such as compact size and fast response/recovery time may find applications in future biochemical and industrial sensing.

Fabrication process and operation principle

Figure 1a,b depict the schematic experimental setup for filling the PCF with the MF (ferromagnetic MNP of 10 nm average size in polyethylene glycol solution from Ferrotec, USA). The flat-cleaved end of a 15 cm PCF was immersed perpendicularly in 2 ml sample vial containing the MF. The MF was successfully infiltrated into the air holes and throughout the whole length of the PCF based on Poiseuille law²⁴ under which the induced pressure gradient between the two ends of the fiber results in a laminar flow of MF [Fig. 1c,d].

Figure 1b shows the SEM cross-section of the used PCF which features a holey cladding made of air holes arranged in a hexagonal lattice pattern with 1.4 mm pitch and average hole diameter of 480 nm. In order to apply a uniform magnetic field on the side of the MF-infiltrated PCF, a plate shaped magnet (KJ Magnetics, USA) was placed next to the sensing region at precisely defined distances from the fiber. A Hall probe-based magnetometer (KOSHAVA 5 model, Wuntronic GmbH) was employed to monitor the magnetic field strength and calibrate the magnetic field fiber-optic sensor. The output beam profile as well as transmitted power at the output of optical fiber were monitored via a CCD camera and optical power meter respectively.

As shown in Fig. 2b, when the infiltrated PCF was exposed to the magnetic field the spatial distribution of MF transforms from randomly homogeneous to an ordered field dependent pattern. The MNPs tend to agglomerate and form chain-like clusters along the direction of magnetic field²⁵ owing to Néel and Brownian relaxation. This phenomenon induces a refractive index (RI) change of the MF that depends on the exerted magnetic field strength^{26,27}.

Results and discussion

It is well known that MFs possesses high optical absorption in the visible spectrum²⁸ as well as a high absorption band at 1470 nm wavelength. The absorption band is related to the orbital transition process in magnetite particles²⁹. Therefore, to benefit from the RI tunability of MF in sensing applications, the geometry of the optical waveguide plays an important role. For example, in the case of a PCF with large air holes, a larger fraction of optical power would be absorbed resulting in very high optical loss. In this work, the use of a special PCF with very small air holes enabled light transmission in the range of 800–1000 nm. The experimental testing setup is depicted in Fig. 2a.

The incident light from a near infrared laser source ($\lambda = 976$ nm, Thorlabs, Pigtailed Butterfly Package) was coupled into the PCF through a combination of objective lenses. The transmitted light power and output beam profiles were recorded via an optical power meter and CCD camera, respectively. A linear polarizer was tuned

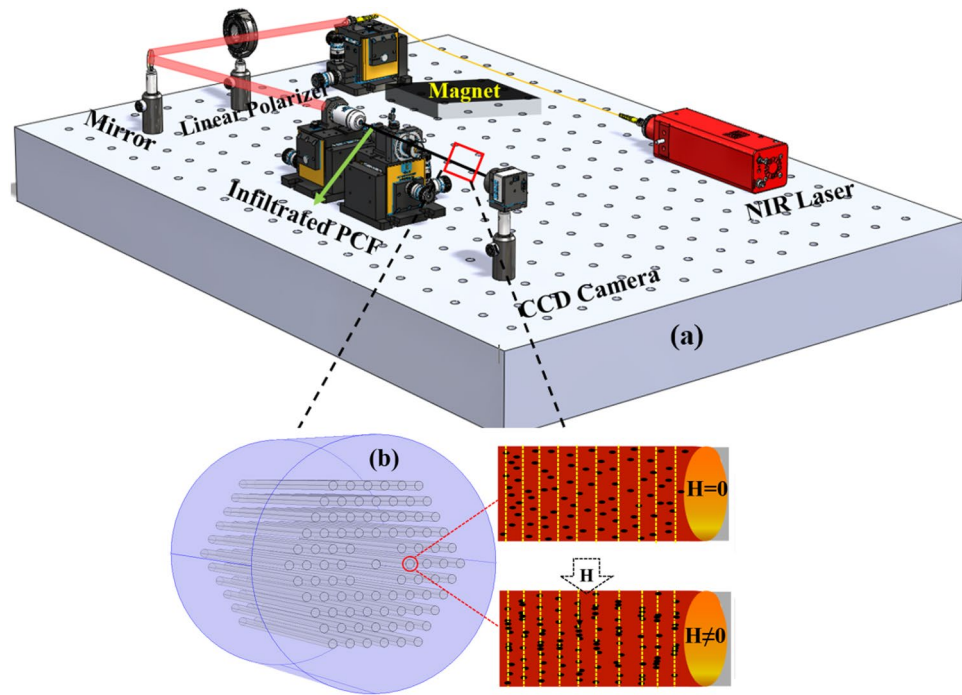


Figure 2. Schematic illustration of (a) experimental setup, (b) magnetic nanoparticles arrangement within the holes of the PCF with (bottom image) and without (top image) the application of an external magnetic field.

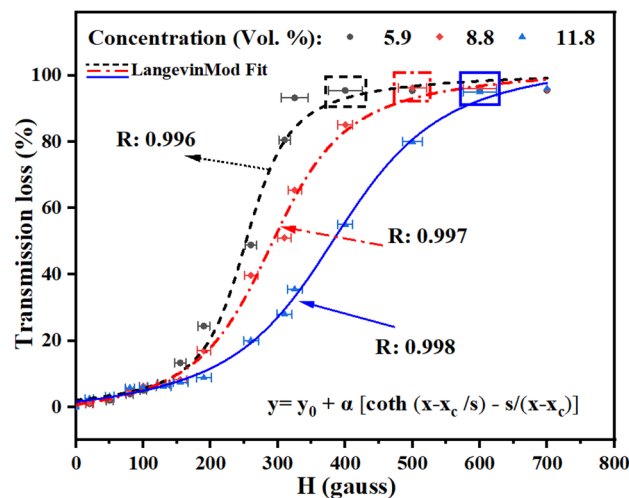


Figure 3. Transmission loss versus magnetic field for samples with various Vol.% concentration of MNPs.

so as to optimize the interaction of light with the MF: when the direction of E-field is parallel to the direction of exerted magnetic field (H) the induced change in optical absorption is almost twice that of the case when the E-field is perpendicular to the direction of applied H-field²⁹.

Influence of MF concentration. The proposed sensor operates based on RI variation and this phenomenon strongly depends on the volume fraction of magnetite particles and the liquid carrier (water, organic solvent, etc.). In this regard, the used polyethylene glycol-based MF with superparamagnetic properties offers higher colloidal stability compared to water based MFs. In this experiment, three different concentrations of MF with 5.9, 8.8 and 11.8 Vol.% of magnetic particles were considered. As shown in Fig. 3 the transmitted optical power through the infiltrated PCF exhibits a strong dependence with the applied magnetic field strength. The sensor saturation point (identified by square markers in Fig. 3) increased with the concentration of MNPs, which is attributed to the saturation magnetization M_s of the MF that follows a linear dependence with the con-

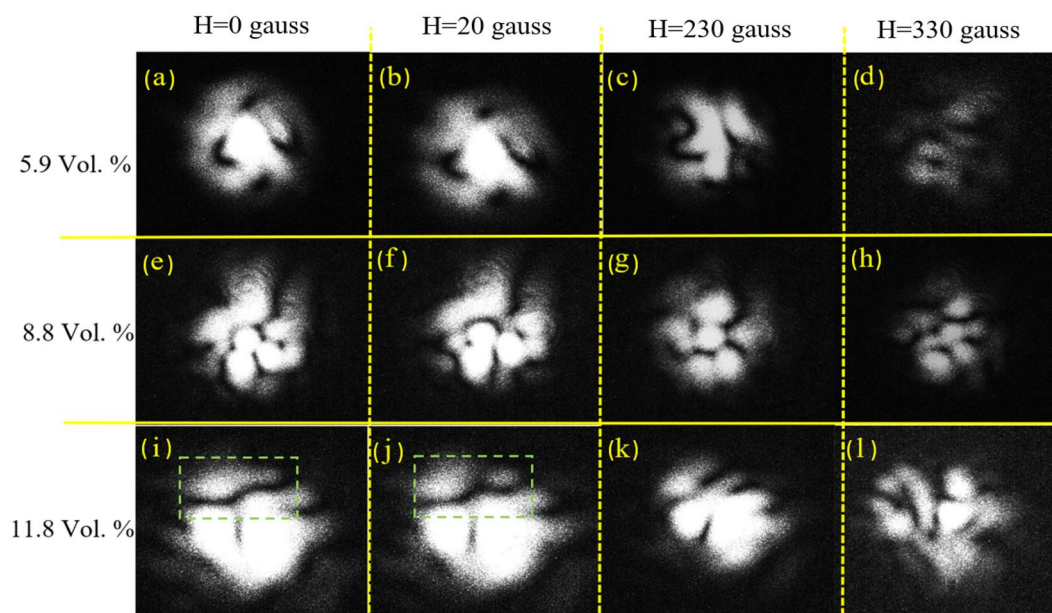


Figure 4. Output beam pattern intensity related to the PCFs infiltrated with: (a–d) 5.9 Vol.%, (e–h) 8.8 Vol.% and (i–l) 11.8 Vol.% concentrations of MNPs under applied magnetic fields of 0, 20, 230 and 330 gauss.

centration. Generally, the magnetization of superparamagnetic materials is described by a Langevin function under magnetic field³⁰.

Correspondingly, the experimental results in Fig. 3 were fitted with a Langevin function with a good degree of confidence ($R \geq 0.996$). The proposed sensor exhibited a limit of detection ≤ 16 gauss within the effective sensing range (i.e. below saturation point). This demonstration of the magnetic-field modulation of transmitted light via the superparamagnetic response of magnetite NPs³¹ points to the potential of using the proposed MF-infiltrated PCF waveguide in magneto-optical sensing applications.

Figure 4 presents the CCD camera images related to the output beam pattern intensity of the infiltrated PCF with various concentrations of MF and submitted under varying magnetic field strengths. This figure provides a clear visual support to the fact depicted in Fig. 3 that transmission losses increase with the applied magnetic field for all three MF concentrations investigated. In the absence of an external magnetic field, individual magnetite particle can be described as a single domain magnetic dipole with permanent moment. While in the presence of low magnetic field (20 gauss), the sensor containing the highest concentration of MNPs showed distinctive pattern changes highlighted by green dashed rectangles in Fig. 4j. An explanation is that at higher volume percentages of MNPs, because the free distance between the centers of two dipoles is lower the portion of attractive polar energy is larger than the thermal energy such that dipole-dipole interactions dominate³². The latter phenomenon results in small RI changes, which in turn leads to the observed variation in the output beam pattern.

Dynamic response of the sensor. The reaction time in sensor applications is an important parameter. In order to evaluate the dynamic response of our sensor, equal length of infiltrated PCFs with different concentrations of MF were exposed to constant magnetic field of 250 ± 8.7 gauss. To ensure the stability and repeatability of sensor responses, the samples were exposed to magnetic field consecutively for three repetitions. The samples containing the lowest concentration of magnetic particles (5.9 Vol%) exhibited very fast response time (time interval during which the transmitted optical power changes from 90 to 10% of its variation) of 0.1s and recovery time (in reverse of response time definition) of also 0.1s as shown in Fig. 5.

Sample with 8.8 Vol. % showed 0.16s response/recovery time. Although MF with the highest concentration (11.8 Vol.%) showed a longer response time of 150s and recovery time of 9s. The latter observed long response time is explained by the growing short-range repulsive forces that increase at high concentration levels of MNPs and which, in turn, slow down the attractive dipole–dipole interactions responsible for the formation of chain-like clusters [depicted in Fig. 2b]. It should be noted that the response and recovery times were not affected by the strength of the applied magnetic field. In Table 1 we summarized the performance of the main sensing specifications reported in the recent literature in comparison to the present work. The compiled results show that the proposed PCF sensor compares favorably in terms of sensitivity and response time.

Sensor output modelling. We also modeled the principal waveguiding mechanism of the infiltrated PCF. Due to the small RI contrast between the silica glass fiber structure and the MF, we expect leakage of the guided light into the holey cladding region, as evidenced by the recorded output intensity patterns in Fig. 4.

In order to model this peculiar waveguiding, finite-element method (FEM) simulations using COMSOL Multiphysics were performed. A uniform 480 nm diameter of PCF holes was assumed along with a pitch value of

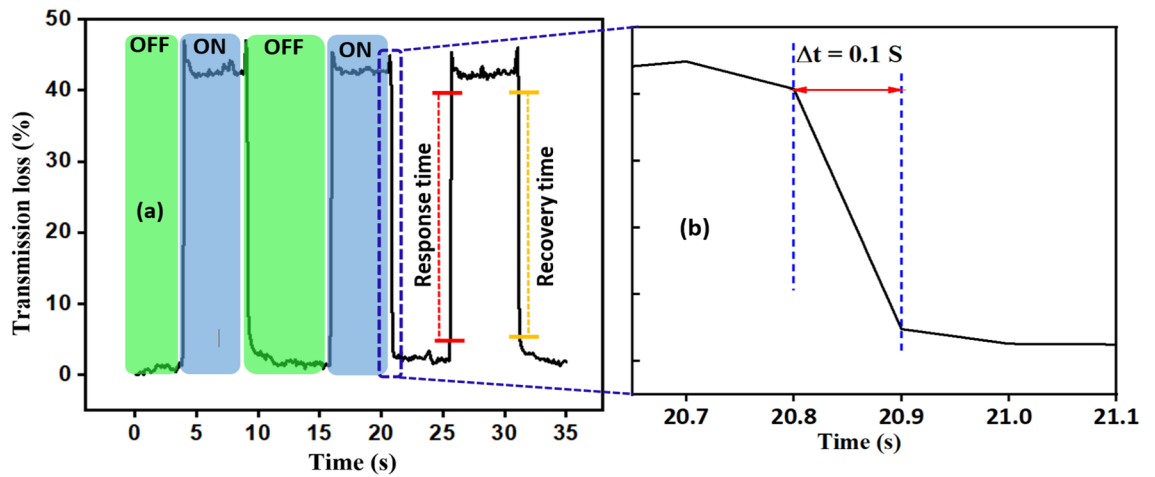


Figure 5. (a) Dynamic response of the infiltrated PCF with 5.9 Vol. % MF in $H=250\pm 8.7$ gauss, (b) Close-up view with finer resolution of the response time region.

Detection mechanism	Optical fiber configuration	Ferrofluid	Detecting range	Response time	Working wavelength (nm)	Ref.
Wavelength shift	eFBG ^a	Synthesized MF based on Fe ₃ O ₄	0–25 mT	15 s	Not mentioned	34
Cladding mode intensity	FBG ^b / TCF ^c	Ferromagnetic Particles	7–15 mT	30 s	1539–1546	35
Wavelength shift	Tapered PCF ^d	EMG 507	10–60 mT	30 min	1550	21
Evanescent waves	POF ^e	Synthesized MF composite	2.5–150 mT	0.7s	550	22
Transmitted power variation	P MZI ^f	EMG 605	0–40 mT	Not mentioned	1550	36
Optical loss	PCF ^g	PBG 300	0–35 mT	0.1 s	976	Present study
Wavelength shift	SNS ^h	EMG 605	4–10 mT	Not mentioned	1530–1560	37

Table 1. Critical parameters in sensing performance based on optical fiber in conjunction with MF for sensing magnetic field. ^aEtched fiber Bragg grating. ^bUniform fiber Bragg grating. ^cThin core fiber. ^dPhotonic crystal fiber. ^ePolymer optical fiber. ^fMach–Zehnder interferometer. ^gPhotonic crystal fiber. ^hSingle mode-no-core-single mode.

1.4 μm inside the 125 μm diameter silica PCF coated with acrylate protective jacket (250 μm diameter). Moreover, the refractive index of different MFs was measured via a digital refractometer (Kruss DR301-95) at 589 nm wavelength. It was observed that the RI increased linearly with increasing concentration of samples. That is for 5.9, 8.8 and 11.7 Vol. % MF the measured RI were 1.4276, 1.4707 and 1.493, respectively.

The latter values of RI were used in the simulations since changes in RI of the MF at 589 nm compared to a wavelength of 976 nm are negligibly small as well as exhibit a similar trend with respect to changes in MF concentration. The first five principal guided modes were selected for each value of applied magnetic field, and the corresponding n_{eff} , loss (α), E-field as well as H-field components were calculated with the FEM mode solver.

Subsequently, the transverse E-field distribution at the output facet of the fiber sensor of length L was modeled as the coherent superposition of the N guided modes as described by the following equation :

$$E_{output}(x, y, \omega) = \sum_{j=1}^{j=N} C_j \cdot E_j(x, y, \omega) e^{(\frac{i\omega}{c})(n_{eff,j})L} e^{-\frac{\alpha_j L}{2}} \tag{1}$$

where $E_j = (E_j^x, E_j^y)$ are the x and y transverse field components, while $n_{eff,j}$ and α_j denote the real effective index and the power loss coefficient of the j – th guided mode at a given frequency ω . The variable C_j stands for the normalized amplitude coupling coefficients calculated from the overlap integral of the input Gaussian beam and overlap integral of the respective modal distributions of the j – th mode :

$$C_j = \frac{1}{4} \int \left[E_j^{x*}(x, y)_{input} \cdot H_j^y(x, y) + E_j^y(x, y) \cdot H_j^{x*}(x, y)_{input} \right] dx dy \tag{2}$$

where the modal fields were properly normalized to unit power through via $\frac{F}{\sqrt{\frac{1}{2} \int \text{Re}(E_i \times H_i^*) dx dy}}$, where F stands for the (E or H) field component of the electromagnetic field vector. The used 976 nm laser is linearly polarized such that an x-polarized Gaussian beam of radius $\sigma = 7\mu m$ was considered as the input source with optical power P : in the simulations:

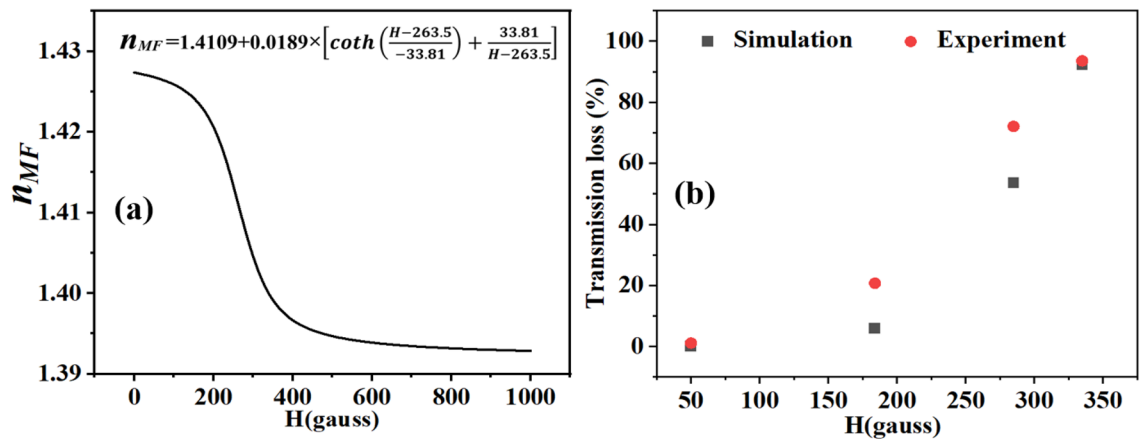


Figure 6. (a) Modeled n_{MF} versus applied magnetic field, (b) Comparison between simulation and experimental data regarding the optical transmission loss in the MF-infiltrated PCF as a function of applied magnetic field.

$$E_{input}(x, y) \approx \hat{x} \cdot \sqrt{\frac{2P}{\pi \sigma^2 n_{clad}}} \exp\left[-\frac{(x^2 + y^2)}{2\sigma^2}\right] \quad (3)$$

$$H_{input}(x, y) \approx \hat{y} \cdot \sqrt{\frac{2P n_{clad}}{\pi \sigma^2}} \exp\left[-\frac{(x^2 + y^2)}{2\sigma^2}\right] \quad (4)$$

Therefore by using Eq. (1) an expression can be derived for the transmitted power in the infiltrated PCF sensor:

$$T_{sensor}(\omega) \approx |E_{output}(x_0, y_0, \omega)| = \left| \sum_{j=1}^{j=N} C_j \cdot E_j(x_0, y_0, \omega) e^{-\frac{i \alpha_{off,j} L}{c}} e^{-\frac{\alpha_j L}{2}} \right| \quad (5)$$

where (x_0, y_0) denotes the coordinates of the PCF cross-section center. In order to model the transmitted power in Eq. (5) of our fiber sensor, we used the FEM-simulated first five dominant guided modes that carry $\geq 90\%$ of the transmitted power. Another key simulation parameter that was considered relates to the changes in the refractive index of the magnetic fluid (n_{MF}) to implement in our simulations when the applied magnetic field is $H > 0$. This relationship between n_{MF} and H is a priori unknown. But knowing that the value of n_{MF} obeys a decreasing Langevin function behavior^{30,33} and the fact that we measured the value of n_{MF} at $H=0$ gauss, we performed a series of FEM simulations that allowed us to find the best fit between the simulated and experimental sensor output transmission loss in Fig. 6b using the model for n_{MF} in Eq. (6) and shown in Fig. 6a. We note that the model in Eq. (6) was derived for a MF concentration of 5.9 Vol.% for which we observed the highest sensor performance. Consequently, all simulations were performed for this specific concentration.

$$n_{MF} = 1.4109 + 0.0189 \times \left[\coth\left(\frac{H - 263.5}{-33.81}\right) + \frac{33.81}{H - 263.5} \right] \quad (6)$$

The discrepancies between the experiment and simulations are owed to additional optical scattering within the PCF that are not accounted for in the simulations which assumed a perfectly smooth PCF structure.

Conclusion

The exquisite precision of mature optical fiber technology in combination with functional fluids tailored with fine magnetic particles makes a hybrid fiber-optic magneto-fluidic probe design desirable for emerging biochemical and environmental sensing applications. In this work, we propose and demonstrate a new type of magnetic field fiber-optic sensor based on a special type of photonic crystal fiber (PCF) with very small submicron-sized air holes infiltrated with a functional magnetic fluid (MF). The resulting fiber-optic probe enabled us to demonstrate a highly sensitive (0–350 gauss), fast (0.1 s response time) and compact magnetic field sensor that can be driven using cost-effective near-infrared laser diodes. The experimental results were well fitted using a Langevin function and explained by a magnetic-field and mode-dependent optical transmission model that was validated by finite-element method simulations. This demonstration provides another step towards novel hybrid magneto-fluidic fiber-optic sensing approaches for biochemical and environmental sensing applications.

Data availability

The datasets used and/or analysed during the current study available from the corresponding author on reasonable request.

Received: 8 March 2022; Accepted: 30 May 2022

Published online: 11 June 2022

References

- Shi, D., Sadat, M. E., Dunn, A. W. & Mast, D. B. Photo-fluorescent and magnetic properties of iron oxide nanoparticles for biomedical applications. *Nanoscale* **7**, 8209–8232 (2015).
- Némeč, F., Morgan, D. D., Gurnett, D. A. & Andrews, D. J. Empirical model of the Martian dayside ionosphere: Effects of crustal magnetic fields and solar ionizing flux at higher altitudes. *J. Geophys. Res. Sp. Phys.* **121**, 1760–1771 (2016).
- Kurosawa, K. Development of fiber-optic current sensing technique and its applications in electric power systems. *Photonic Sensors* **4**, 12–20 (2014).
- Mancoff, F. B., Dunn, J. H., Clemens, B. M. & White, R. L. A giant magnetoresistance sensor for high magnetic field measurements. *Appl. Phys. Lett.* **77**, 1879–1881 (2000).
- Langfelder, G. & Tocchio, A. Operation of Lorentz-force MEMS magnetometers with a frequency offset between driving current and mechanical resonance. *IEEE Trans. Magn.* **50**, 1–6 (2013).
- Snoei, M. F., Schaffer, V., Udayashankar, S. & Ivanov, M. V. Integrated fluxgate magnetometer for use in isolated current sensing. *IEEE J. Solid-State Circuits* **51**, 1684–1694 (2016).
- Ripka, P. & Janosek, M. Advances in magnetic field sensors. *IEEE Sens. J.* **10**, 1108–1116 (2010).
- Koo, K. P. & Sigel, G. H. Characteristics of fiber-optic magnetic-field sensors employing metallic glasses. *Opt. Lett.* **7**, 334–336 (1982).
- Rashleigh, S. C. Magnetic-field sensing with a single-mode fiber. *Opt. Lett.* **6**, 19–21 (1981).
- Sedlar, M., Matejec, V. & Paulicka, I. Optical fibre magnetic field sensors using ceramic magnetostrictive jackets. *Sens. Actuators A* **84**, 297–302 (2000).
- Yoshino, T. & Ohno, Y. Highly sensitive all-optical method for measuring magnetic fields. *Fiber Integr. Opt.* **3**, 391–399 (1981).
- Horng, H.-E. *et al.* Magneto-optics resulted from optical gratings of magnetic fluid films subjected to perpendicular magnetic fields. *J. Appl. Phys.* **88**, 5904–5908 (2000).
- Horng, H.-E. *et al.* Tunable optical switch using magnetic fluids. *Appl. Phys. Lett.* **85**, 5592–5594 (2004).
- Chieh, J.-J., Yang, S.-Y., Horng, H.-E., Hong, C.-Y. & Yang, H.-C. Magnetic-fluid optical-fiber modulators via magnetic modulation. *Appl. Phys. Lett.* **90**, 133505 (2007).
- Dutt, A., Varshney, S. K. & Mahapatra, S. Design of tunable couplers using magnetic fluid filled three-core optical fibers. *IEEE Photonics Technol. Lett.* **24**, 164–166 (2011).
- Wu, W. *et al.* Compact magnetic field sensor based on a magnetic-fluid-integrated fiber interferometer. *IEEE Magn. Lett.* **10**, 1–5 (2019).
- Philip, J. & Laskar, J. M. Optical properties and applications of ferrofluids—a review. *J. Nanofluids* **1**, 3–20 (2012).
- Jin, J., Song, D., Geng, J. & Jing, D. Time-dependent scattering of incident light of various wavelengths in ferrofluids under external magnetic field. *J. Magn. Magn. Mater.* **447**, 124–133 (2018).
- Hu, T., Zhao, Y., Li, X., Chen, J. & Lv, Z. Novel optical fiber current sensor based on magnetic fluid. *Chin. Opt. Lett.* **8**, 392–394 (2010).
- Lv, R.-Q., Zhao, Y., Wang, D. & Wang, Q. Magnetic fluid-filled optical fiber Fabry–Pérot sensor for magnetic field measurement. *IEEE Photonics Technol. Lett.* **26**, 217–219 (2014).
- Zhao, Y., Wu, D. & Lv, R.-Q. Magnetic field sensor based on photonic crystal fiber taper coated with ferrofluid. *IEEE Photonics Technol. Lett.* **27**, 26–29 (2015).
- Azad, S., Nikzad, A. & Parvizi, R. evanescent field-modulated magnetic immune sensor based on magnetic fluid and polymer optical fiber. *IEEE Sens. J.* **2**, 2 (2018).
- Gao, R., Jiang, Y. & Abdelaziz, S. J. All-fiber magnetic field sensors based on magnetic fluid-filled photonic crystal fibers. *Opt. Lett.* **38**, 1539–1541 (2013).
- Pfützner, J. Poiseuille and his law. *Anaesthesia* **31**, 273–275 (1976).
- Kötitz, R., Fannin, P. C. & Trahms, L. Time domain study of Brownian and Néel relaxation in ferrofluids. *J. Magn. Magn. Mater.* **149**, 42–46 (1995).
- Yang, S.-Y. *et al.* Magnetically-modulated refractive index of magnetic fluid films. *Appl. Phys. Lett.* **81**, 4931–4933 (2002).
- Horng, H.-E., Hong, C.-Y., Yang, S.-Y. & Yang, H.-C. Designing the refractive indices by using magnetic fluids. *Appl. Phys. Lett.* **82**, 2434–2436 (2003).
- Hoffmann, B. & Köhler, W. Reversible light-induced cluster formation of magnetic colloids. *J. Magn. Magn. Mater.* **262**, 289–293 (2003).
- Inaba, N., Miyajima, H., Takahashi, H., Taketomi, S. & Chikazumi, S. Magneto-optical absorption in infrared region for magnetic fluid thin film. *IEEE Trans. Magn.* **25**, 3866–3868 (1989).
- Bean, C. P. & Livingston, U. D. Superparamagnetism. *J. Appl. Phys.* **30**, S120–S129 (1959).
- Sharma, M., Pradhan, P. & Ung, B. Endlessly mono-radial annular core photonic crystal fiber for the broadband transmission and supercontinuum generation of vortex beams. *Sci. Rep.* **9**, 2488 (2019).
- Zhu, Y., Ivey, M. L., Sheaffer, P., Pousset, J. & Liu, J. Magnetic field-induced phase transitions in ferrofluid emulsion. *Int. J. Mod. Phys. B* **10**, 2973–2981 (1996).
- Zhao, Y., Lv, R.-Q., Wang, D. & Wang, Q. Fiber optic Fabry–Perot magnetic field sensor with temperature compensation using a fiber Bragg grating. *IEEE Trans. Instrum. Meas.* **63**, 2210–2214 (2014).
- Dai, J., Yang, M., Li, X., Liu, H. & Tong, X. Magnetic field sensor based on magnetic fluid clad etched fiber Bragg grating. *Opt. Fiber Technol.* **17**, 210–213 (2011).
- Tian, Q. *et al.* A temperature-independent fibre-optic magnetic-field sensor using thin-core fibre tailored fibre Bragg grating. *Opt. Commun.* **393**, 169–172 (2017).
- Wu, J. *et al.* Magnetic-field sensor based on core-offset tapered optical fiber and magnetic fluid. *J. Opt.* **16**, 075705 (2014).
- Chen, Y., Han, Q., Liu, T., Lan, X. & Xiao, H. Optical fiber magnetic field sensor based on single-mode-multimode-single-mode structure and magnetic fluid. *Opt. Lett.* **38**, 3999–4001 (2013).

Acknowledgements

The authors would like to thank Mathieu Gratuze for his help in the extraction of simulation data.

Author contributions

S.A., B.U. and R.I. conceived the experiments. S.A. and S.K.M. conducted the experiments. B.U., S.A. and G.R. worked on the modelling and interpretation of the results. B.U. and R.I. supervised the project as well as provided the resources. All authors reviewed the manuscript.

Competing interests

The authors declare no competing interests.

Additional information

Correspondence and requests for materials should be addressed to B.U.

Reprints and permissions information is available at www.nature.com/reprints.

Publisher's note Springer Nature remains neutral with regard to jurisdictional claims in published maps and institutional affiliations.



Open Access This article is licensed under a Creative Commons Attribution 4.0 International License, which permits use, sharing, adaptation, distribution and reproduction in any medium or format, as long as you give appropriate credit to the original author(s) and the source, provide a link to the Creative Commons licence, and indicate if changes were made. The images or other third party material in this article are included in the article's Creative Commons licence, unless indicated otherwise in a credit line to the material. If material is not included in the article's Creative Commons licence and your intended use is not permitted by statutory regulation or exceeds the permitted use, you will need to obtain permission directly from the copyright holder. To view a copy of this licence, visit <http://creativecommons.org/licenses/by/4.0/>.

© The Author(s) 2022